

## Predicting the Rossby number in convective experiments

EVAN H. ANDERS,<sup>1,2</sup> CATHRYN M. MANDUCA,<sup>2</sup> BENJAMIN P. BROWN,<sup>1,2</sup> JEFFREY S. OISHI,<sup>3</sup> AND GEOFFREY M. VASIL<sup>4</sup>

<sup>1</sup>*Dept. Astrophysical & Planetary Sciences, University of Colorado – Boulder, Boulder, CO 80309, USA*

<sup>2</sup>*Laboratory for Atmospheric and Space Physics, Boulder, CO 80303, USA*

<sup>3</sup>*Department of Physics and Astronomy, Bates College, Lewiston, ME 04240, USA*

<sup>4</sup>*University of Sydney School of Mathematics and Statistics, Sydney, NSW 2006, Australia*

(Received October 19, 2018; Revised December 28, 2018; Accepted ??)

Submitted to ApJ

### ABSTRACT

The Rossby number is a crucial parameter describing the degree of rotational constraint on the convective dynamics in stars and planets. However, it is not an input to computational models of convection but must be measured ex post facto. Here, we report the discovery of a new quantity, the Predictive Rossby number, which is both tightly correlated with the Rossby number and specified in terms of common inputs to numerical models. The Predictive Rossby number can be specified independent of Rayleigh number, allowing suites of numerical solutions to separate the degree of rotational constraint from the strength of the driving of convection. We examine the scaling of convective transport in terms of the Nusselt number and the degree of turbulence in terms of the Reynolds number of the flow, and we find scaling laws nearly identical to those in nonrotational convection at low Rossby number when the Predictive Rossby number is held constant. Finally, we describe the boundary layers as a function of increasing turbulence at constant Rossby number.

*Keywords:* convection — hydrodynamics — turbulence — dynamo — Sun: rotation

### 1. INTRODUCTION

Rotation influences the dynamics of convective flows in stellar and planetary atmospheres. Many studies on the fundamental nature of rotating convection in both laboratory and numerical settings have provided great insight into the properties of convection in both the rapidly rotating regime and the transition to the rotationally unconstrained regime (King et al. 2009; Zhong et al. 2009; Schmitz & Tilgner 2009; King et al. 2012; Julien et al. 2012; King et al. 2013; Ecke & Niemela 2014; Stellmach et al. 2014; Cheng et al. 2015; Gastine et al. 2016). The scaling behavior of heat transport, the nature of convective flow structures, and the importance of boundary layer-bulk interactions in driving dynamics are well known. Yet, we do not know of any simple procedure for predicting the magnitude of vortical flow

gradients purely from experimental control parameters, such as bulk rotation rate and thermal input.

In the astrophysical context, many studies of rotating convection have investigated questions inspired by the solar dynamo (Glatzmaier & Gilman 1982; Busse 2002; Brown et al. 2008, 2010, 2011; Augustson et al. 2012; Guerrero et al. 2013; Käpylä et al. 2014). Even when these simulations nominally rotate at the solar rate, they frequently produce distinctly different behaviors than the true Sun, such as anti-solar differential rotation profiles (Gastine et al. 2014; Brun et al. 2017). It seems that these differences occur because the simulations produce less rotationally constrained states than the Sun. The influence of rotation results from the local shear gradients, and these are not direct input parameters. Recent simulations predict significant rotational influence in the deep solar interior, which can drastically affect flows throughout the solar convection zone (Featherstone & Hindman 2016; Greer et al. 2016). In the planetary context, the balance between magnetic and rotational forces likely leads to the observed differences between ice giant and gas giant dynamos in our solar system (Soderlund

et al. 2015). The work of Aurnou & King (2017) demonstrates the importance of studying a dynamical regime with the proper balance between Lorentz, Coriolis, and inertial forces when modeling astrophysical objects such as planetary dynamos.

In short, simulations must achieve the proper rotational balance if they are to explain the behavior of astrophysical objects. In Boussinesq studies, rotational constraint is often measured by comparing dynamical and thermal boundary layers or deviation in heat transport from the non-rotating state (King et al. 2012; Julien et al. 2012; King et al. 2013). Such measurements are not available for astrophysical objects, where the degree of rotational influence is best assessed by the ratio between nonlinear advection magnitude and the linear Coriolis accelerations. The *Rossby number* is the standard measure of this ratio,

$$\text{Ro} \equiv \frac{|\nabla \times \mathbf{u}|}{2|\mathbf{\Omega}|} \sim \frac{|(\nabla \times \mathbf{u}) \times \mathbf{u}|}{|2\mathbf{\Omega} \times \mathbf{u}|}, \quad (1)$$

where  $\mathbf{\Omega}$  denotes the bulk rotation vector. Many proxies for the dynamical Rossby number exist that are based solely on input parameters, most notably the *convective* Rossby number. However, all proxies produce imperfect predictions for the true dynamically relevant quantity.

*In this letter, we demonstrate an empirical method of predicting the output Rossby number of convection in a simple stratified system.*

In Anders & Brown (2017) (hereafter AB17), we studied non-rotating compressible convection without magnetic fields in polytropic atmospheres. In this work, we extend AB17 to rotationally-influenced, *f*-plane atmospheres (e.g., Brummell et al. 1996, 1998; Calkins et al. 2015). We determine how the input parameters we studied previously, which controlled the Mach and Reynolds numbers of the evolved flows, couple with the Taylor number (Ta, Julien et al. 1996), which sets the magnitude of the rotational vector.

In section 2, we describe our experiment and paths through parameter space. In section 3, we present the results of our experiments and in section 4 we offer concluding remarks.

## 2. EXPERIMENT

We study fully compressible, stratified convection under precisely the same atmospheric model as in AB17, but here we have included rotation. We study polytropic atmospheres with  $n_p = 3$  density scale heights and a superadiabatic excess of  $\epsilon = 10^{-4}$  such that flows are at low Mach number. We study a domain in which

the gravity,  $\mathbf{g} = -g\hat{z}$ , and rotational vector,  $\mathbf{\Omega} = \Omega\hat{z}$ , are antiparallel (as in e.g., Julien et al. 1996; Brummell et al. 1996).

We evolve the velocity ( $\mathbf{u}$ ), temperature ( $T$ ), and log density ( $\ln \rho$ ) according to the Fully Compressible Navier-Stokes equations in the same form presented in AB17, with the addition of the Coriolis term,  $2\mathbf{\Omega} \times \mathbf{u}$ , to the left-hand side of the momentum equation. We impose impenetrable, stress-free, fixed-temperature boundary conditions at the top and bottom of the domain.

We specify the kinematic viscosity ( $\nu$ ), thermal diffusivity ( $\chi$ ), and strength of rotation ( $\Omega$ ) at the top of the domain by choosing the Rayleigh number (Ra), Prandtl number (Pr), and Taylor number (Ta),

$$\text{Ra} = \frac{gL_z^3 \Delta S / c_P}{\nu \chi}, \quad \text{Pr} = \frac{\nu}{\chi}, \quad \text{Ta} = \left( \frac{2\Omega L_z^2}{\nu} \right)^2, \quad (2)$$

where  $L_z$  is the depth of the domain as defined in AB17,  $\Delta S \propto \epsilon n_p$  is the specific entropy difference between the top and bottom of the atmosphere, and the specific heat at constant pressure is  $c_P = \gamma/(\gamma - 1)$  with  $\gamma = 5/3$ . Throughout this work we set  $\text{Pr} = 1$ . The Taylor number relates to the often-quoted Ekman number by the equality  $\text{Ek} \equiv \text{Ta}^{-1/2}$ .

Due to stratification, Ra and Ta both grow with depth as  $(\text{Ra}, \text{Ta}) \propto \rho^2$  (see AB17). We nondimensionalize our atmospheres at the top of the domain, and so all values of Ra and Ta quoted in this work are the minimal value of Ra and Ta in the domain at  $z = L_z$ . For direct comparison to Boussinesq studies, past work has found that the value of Ra at the atmospheric midplane ( $z = L_z/2$ ) varies minimally with increasing stratification (Unno et al. 1960). For the atmospheres presented in this work, midplane Ra and Ta values are larger than reported top-of-atmosphere values by a factor of  $\sim 70$ , and values at the bottom of the atmosphere are larger by  $\sim 400$ .

When Ta is large, the wavenumber of convective onset increases according to  $k_{\text{crit}} \propto \text{Ta}^{1/6}$  (Chandrasekhar 1961; Calkins et al. 2015). We study horizontally-periodic, 3D Cartesian domains with extents of  $x, y = [0, 4(2\pi/k_{\text{crit}})]$  and  $z = [0, L_z]$ . At large values of Ta, these domains are tall and skinny, as in Stellmach et al. (2014). We evolve our simulations using the Dedalus<sup>1</sup> pseudospectral framework, and our numerical methods are identical to those presented in AB17. The supplemental materials of this paper include a `.tar` file which

<sup>1</sup> <http://dedalus-project.org/>

contains the code used to perform the simulations in this work.

The critical value of  $Ra$  at which rapidly rotating convection onsets also depends on  $Ta$  (see the black line in figure 1a), roughly according to  $Ra_{\text{crit}} \sim Ta^{2/3}$  (Chandrasekhar 1961; Calkins et al. 2015). Even taking account of linear theory, the dependence of the evolved nonlinear fluid flows on the input parameters makes predicting the rotational constraint very challenging. We will explore three paths through  $Ra$ - $Ta$  space:

$$Ra = \begin{cases} \mathcal{S} Ra_{\text{crit}}(Ta), & \text{(I)} \\ (Ro_c)^2 Pr Ta, & \text{(II)} \\ (Ro_p)^2 Pr^{1/2} Ta^{3/4} & \text{(III).} \end{cases} \quad (3)$$

Paths on constraint I are at constant supercriticality,  $\mathcal{S} \equiv Ra/Ra_{\text{crit}}$  (blue dash-dot line in figure 1a). Paths on constraint II (green dashed line in figure 1a) are at a constant value of the classic *convective* Rossby number,

$$Ro_c = \sqrt{\frac{Ra}{Pr Ta}} = \frac{1}{2\Omega} \sqrt{\frac{g \Delta S}{c_p L_z}}, \quad (4)$$

which has provided (e.g., Julien et al. 1996; Brummell et al. 1996) a common proxy for the degree of rotational constraint. This parameter measures the importance of buoyancy relative to rotation without involving dissipation. Paths on constraint III (e.g., orange solid lines in figure 1a) set constant a ratio which we call the “Predictive Rossby number,”

$$Ro_p = \sqrt{\frac{Ra}{Pr^{1/2} Ta^{3/4}}} = \frac{1}{(2\Omega)^{3/4}} \sqrt{\frac{g \Delta S}{c_p \chi^{1/2}}} \quad (5)$$

Unlike paths through parameter space which hold  $Ro_c$  constant, paths with constant  $Ro_p$  feel changes in diffusivities but not the depth of the domain. To our knowledge, these paths have not been reported in the literature, although the importance of  $Ra/Ta^{3/4} = Ra Ek^{3/2}$  has been independently found by King et al. (2012) using a boundary layer analysis. We compare our results to their theory in Section 4.

In this work, we primarily study three values of  $Ro_p$ . These values are shown in Fig. 1a and Table 1. Table 1 lists the values of  $(Ra_{\text{crit}}, Ta_{\text{crit}})$  for each value of  $Ro_p$ , and also the maximum value of  $(Ra, Ta)$  studied in this work for each path. We additionally walked two pathways at constant supercriticality (constraint I,  $\mathcal{S} = \{2, 3\}$ ) and three pathways at constant convective Rossby number (constraint II,  $Ro_c = \{1, 0.3, 0.1\}$ ). Full details on all cases are provided in Appendix A and the supplemental materials.

**Table 1.** Parameter space

$Ro_p$	$(Ra_{\text{crit}}, Ta_{\text{crit}})$	$(Ra_{\text{max}}, Ta_{\text{max}})$
0.60	$(10^{4.88}, 10^{7.10})$	$(10^{9.09}, 10^{12.72})$
0.96	$(10^{2.44}, 10^{3.30})$	$(10^{8.58}, 10^{11.49})$
1.58	$(10^{1.39}, 10^{1.33})$	$(10^{7.14}, 10^{8.99})$

NOTE— Values of the critical  $Ra$  and  $Ta$  for each  $Ro_p$  track are reported, as well as the maximal values of  $Ra$  and  $Ta$  studied on each track. All values reported are for the top of the atmosphere. A fuller set of simulations are reported in Table 2 with midplane  $Ra$  and  $Ta$  values as well.

### 3. RESULTS

In our stratified domains, for  $Ta \geq 10^5$ , a best-fit to results from a linear stability analysis provides  $Ra_{\text{crit}} = 1.459Ta^{2/3}$  and  $k_{\text{crit}} = 0.414Ta^{1/6}$  for direct onset of convection. In figure 1a, the value of  $Ra_{\text{crit}}(Ta)$  is shown. Sample paths for each criterion in equation 3 through this parameter space are also shown. In figure 1b, we display the evolution of  $Ro$  with increasing  $Ra$  along various paths through parameter space. We find that  $Ro$  increases on constant  $Ro_c$  paths, decreases on constant  $\mathcal{S}$  paths, and remains roughly constant along constant  $Ro_p$  paths. In figure 1c, the value of  $Ro$  is shown simultaneously as a function of  $Ro_p$  and  $Ro_c$  for all experiments conducted in this study. We find a general power-law of the form  $Ro = C Ro_c^\alpha Ro_p^\beta$ . In the rotationally-dominated regime where  $Ro < 0.2$  and  $Re_\perp > 5$  (see Eqn. 6), we find  $\alpha = -0.02$ , and  $Ro$  can be said to be a function of  $Ro_p$  alone. Under this assumption, we report a scaling of  $Ro = (0.148 \pm 0.003) Ro_p^{3.34 \pm 0.07}$ . In the less rotationally dominated regime of  $Ro > 0.2$  and  $Re_\perp > 5$ , we find  $\{C, \alpha, \beta\} = \{0.2, -0.19, 1.5\}$ .

In figure 2, sample snapshots of the evolved entropy field in the  $x$ - $y$  plane near the top and at the middle of the domain are shown. In the left column, flows are at  $Ro \sim 1$  and resemble the classic granular structure of nonrotating convection (see e.g., figure 2 in AB17), where strong narrow downflow lanes punctuate broad upwellings. The narrow downflows at the top organize themselves into intense coherent structures at the midplane, and at the midplane the downflows have much stronger entropy fluctuations than the broad and slower upflows.

$Ro$  decreases from left to right into the rotationally constrained regime. As  $Ro$  decreases, the narrow downflow lanes begin to disappear and the flows at midplane become more symmetric. In the rotationally constrained

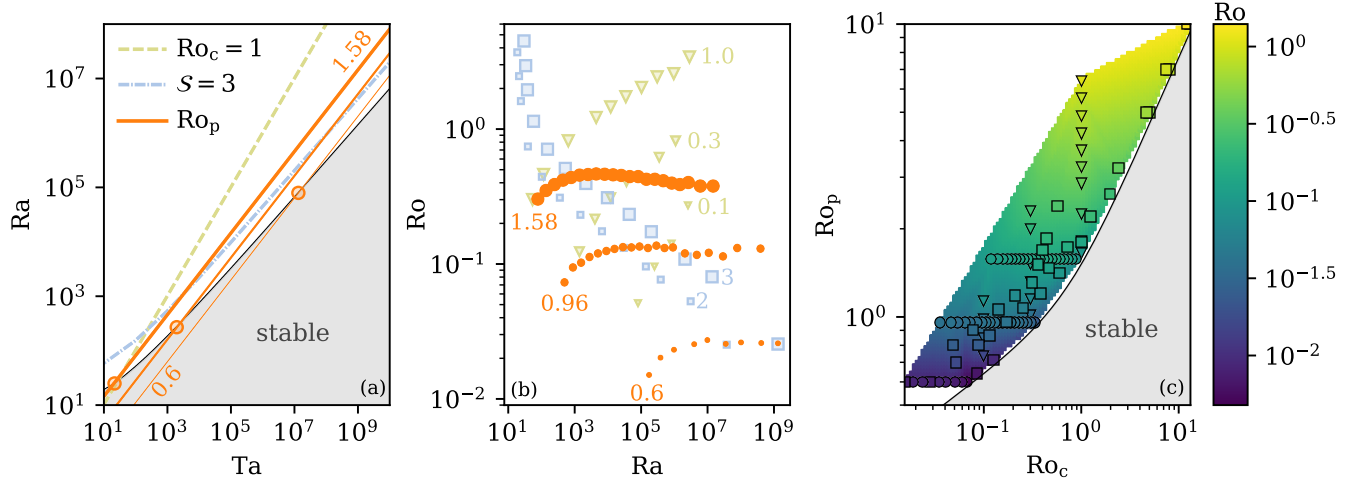


**Figure 1.** (a) The critical Rayleigh number, as a function of the Taylor number, is plotted as a solid black line. The grey shaded region is subcritical, and rotation suppresses convection there. Paths of constant Convective Rossby number ( $Ro_c$ , green dashed line), constant supercriticality ( $S$ , blue dash-dot line), and constant Predictive Rossby number ( $Ro_p$ , orange solid lines) are shown. From thickest to thinnest, paths with  $Ro_p = [1.58, 0.96, 0.6]$  are plotted, and the value of  $(Ta_{crit}, Ra_{crit})$  for each path is denoted by a circular marker (see Table 1). (b) Evolved  $Ro$  is plotted vs.  $Ra$  along paths of  $Ro_p = [1.58, 0.96, 0.6]$  for [big, medium, small] orange circles. For comparison, paths of constant  $S$  (blue squares,  $S = [3, 2]$  for [big, small] squares) and constant  $Ro_c$  (green triangles,  $Ro_c = [1, 0.3, 0.1]$  for [big, medium, small] triangles) are shown. (c) The evolved value of  $Ro$  is shown as a function of  $Ro_p$  and  $Ro_c$ . Each of the experiments in (b) is outlined by a black (circle, triangle, square) for points along constant ( $Ro_p, Ro_c, S$ ) paths. The color inside of the marker represents the exact measured  $Ro$  of that experiment, while the colormap outside of markers is a linear interpolation of the data set.

regime ( $Ro \sim 0.03$ ), the convective structures are distinctly different. Here we observe dynamically persistent, warm upflow columns surrounded by bulk weak downflow regions. At the midplane, the upflow columns have substantially higher entropy perturbations than the surrounding weak downflows which sheathe them, and the locations of the columns are tightly correlated with their positions at the top of the domain. These quasi-two-dimensional dynamics are similar to those seen in rapidly rotating Rayleigh-Bénard convection (e.g., [Stellmach et al. 2014](#)). The select cases displayed in figure 2 each have an evolved volume-averaged  $Re_{\perp} \approx 32$  (defined below in equation 6).

We measure the Nusselt number ( $Nu$ ), which quantifies heat transport in a convective solution, as defined in [AB17](#). In figure 3a, we plot  $Nu$  as a function of  $Ra/Ra_{crit}$  at fixed  $Ro_p$ . We find that  $Nu \propto \{Ra^{0.29 \pm 0.01}, Ra^{0.29 \pm 0.01}, Ra^{0.24}\}$  for  $Ro_p = \{0.6, 0.957, 1.58\}$ . In the regime of  $Ro \lesssim 0.1$ , these scaling laws are indistinguishable from a classic  $Ra^{2/7}$  power law scaling, which is observed in nonrotating Rayleigh-Bénard and stratified convection ([Ahlers et al. 2009, AB17](#)). Our results seem consistent with the stress-free, rotating Rayleigh-Bénard convection results of [Schmitz & Tilgner \(2009\)](#), whose re-arranged Eqn. 7 returns a best-fit of  $Nu \propto Ra^{0.26}$  at fixed  $Ro_p$ . Their work primarily spans the transition regime between ro-

tationally constrained and unconstrained convection, and so it is perhaps not surprising that their power law is a blend of our rotationally-constrained  $Ra^{2/7}$  power law and the fairly rotationally unconstrained  $Ra^{0.24}$  at  $Ro_p = 1.58$ .

Flows are distinctly different parallel to and perpendicular from the rotation vector, which aligns with gravity and stratification. We measure two forms of the RMS Reynolds number,

$$Re_{\parallel} = \frac{|\mathbf{u}|L_z}{\nu}, \quad Re_{\perp} = \frac{|\mathbf{u}|}{\nu} \frac{2\pi}{k_{crit}}, \quad (6)$$

where the length scale in  $Re_{\perp}$  is the wavelength of convective onset, and is related to the horizontal extent of our domain (see section 2). From our work in [AB17](#), we expect the RMS velocity to scale as  $|\mathbf{u}| \propto \sqrt{\Delta S}$ . By definition,  $\nu \propto \sqrt{Ra}/(\text{Pr} \Delta S)$ , and  $L_z$  is a constant set by the stratification while  $k_{crit} \propto Ta^{1/6}$ . Along paths of constant  $Ro_p$ , we thus expect  $Re_{\parallel} \propto Ra^{1/2}$  and  $Re_{\perp} \propto Ra^{5/18}$  when  $\text{Pr}$  is held constant.

In figure 3b, we plot  $Re_{\parallel}$  and  $Re_{\perp}$  as a function of  $Ra/Ra_{crit}$  at fixed  $Ro_p$ . We find that  $Re_{\parallel} \propto \{Ra^{0.44 \pm 0.01}, Ra^{0.45 \pm 0.01}, Ra^{0.44}\}$  and  $Re_{\perp} \propto \{Ra^{0.22 \pm 0.01}, Ra^{0.23 \pm 0.01}, Ra^{0.21}\}$  for  $Ro_p = \{0.6, 0.957, 1.58\}$ . These scalings are similar to but slightly weaker than our predictions in all cases. However, the scaling of  $Re_{\parallel} \propto Ra^{0.45}$ , is once again a power law observed fre-



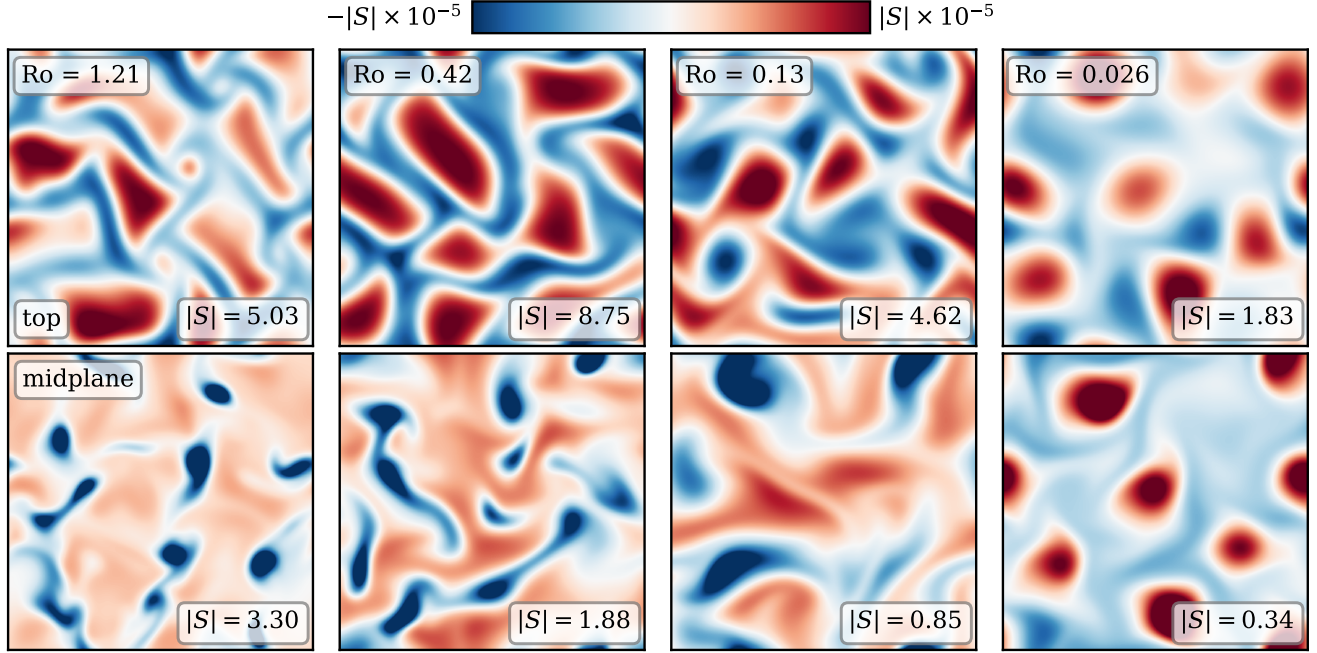


**Figure 2.** Horizontal slices of the evolved entropy deviation from the mean at  $z = 0.95L_z$  (top row) and  $z = 0.5L_z$  (bottom row) are shown for select simulations. All runs displayed here have an evolved volume-averaged  $Re_{\perp} \approx 32$ . As  $Ro$  decreases from  $O(1)$  on the left to  $O(0.03)$  on the right, and thus the rotational constraint on the flow increases, significant changes in flow morphology are observed. As  $Ro$  decreases, Coriolis forces more effectively deflect the convective flows, and the classic granular convective pattern gives way to vortical columns that are quasi-two-dimensional.

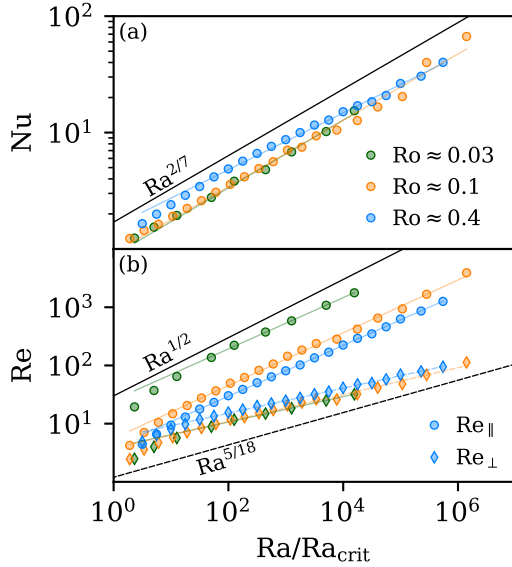


**Figure 3.** Scaling laws for paths at  $Ro_p = 1.58$  ( $Ro \approx 0.4$ ),  $Ro_p = 0.96$  ( $Ro \approx 0.1$ ), and  $Ro_p = 0.6$  ( $Ro \approx 0.03$ ) are shown. Numbers are plotted vs.  $Ra/Ra_{crit}$ , where  $Ra_{crit}$  is given in Table 1. (a)  $Nu$ , as defined in AB17, is shown. (b)  $Re_{\parallel}$  and  $Re_{\perp}$ , as defined in equation 6, are shown. All values of  $Ro_p$  trace out similar  $Nu$  and  $Re_{\perp}$  tracks, whereas  $Re_{\parallel}$  tracks shift upwards as  $Ro$  decreases.

quently in nonrotating convection (Ahlers et al. 2009, AB17). We also observe that  $Re_{\perp}$  collapses for each  $Ro_p$  track, while  $Re_{\parallel}$  experiences an offset to larger values as  $Ro_p$  shrinks. The offset in  $Re_{\parallel}$  is unsurprising, because more rotationally constrained flows result in smaller boundary layers relative to the vertical extent of our stratified domain. The horizontal extent of our domain scales with the strength of rotation, and so regardless of  $Ro_p$ , flows perpendicular to the rotational and buoyant direction are comparably turbulent at the same  $Ra/Ra_{crit}$ . We find  $Re_{\perp}$  and  $Re_{\parallel}$  are, respectively, good proxies for the horizontal and perpendicular resolution required to resolve an experiment.

Figure 4 shows time- and horizontally-averaged profiles of  $Ro$  and the standard deviation of the entropy,  $\sigma_s$ . Figures 4a&b show these profiles for  $Ro_p = 1.58$  ( $Ro \approx 0.4$ ), while Figures 4c&d show these profiles for  $Ro_p = 0.96$  ( $Ro \approx 0.1$ ). The transition in profile behavior from low  $Ra$  (yellow) to high  $Ra$  (purple) is denoted by the color of the profile. As  $Ra$  increases at a constant value of  $Ro_p$ , both the thermal ( $\sigma_s$ ) and dynamical ( $Ro$ ) boundary layers become thinner. We measure the thickness of the thermal boundary layer ( $\delta_s$ ) at the top of the domain by finding the location of the first maxima of  $\sigma_s$  away from the boundary. We measure the thickness of

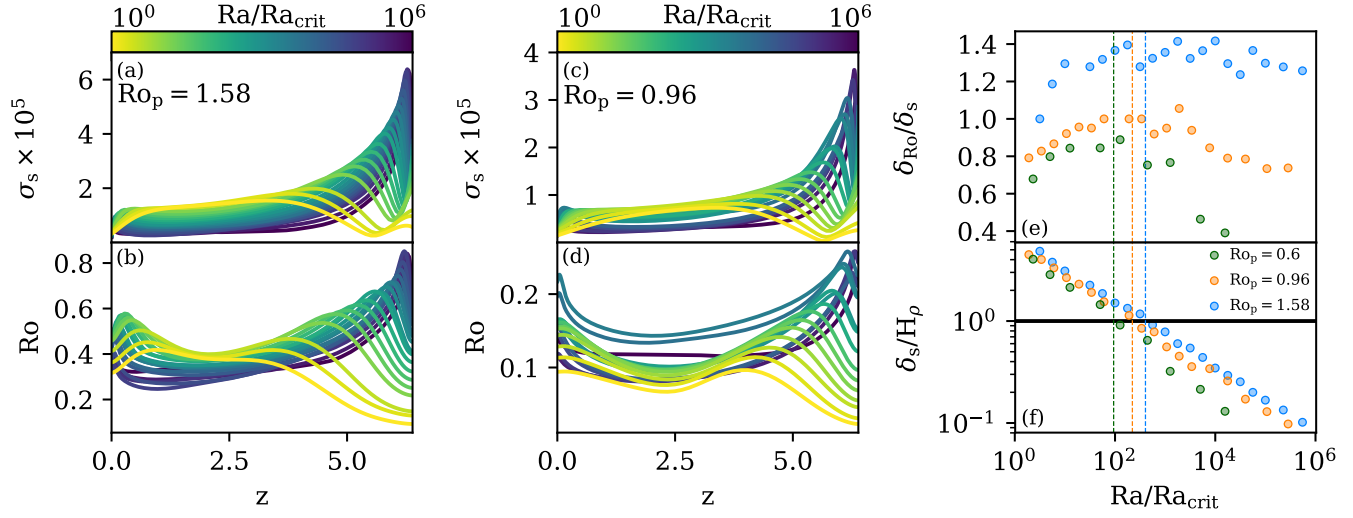


**Figure 4.** Horizontally-averaged profiles of the standard deviation of entropy ( $\sigma_s$ , a) and Rossby number ( $Ro$ , b) are shown vs. height for  $Ro_p = 1.58$  ( $Ro \approx 0.4$ ). Similar profiles are shown in (c) and (d) for  $Ro_p = 0.96$  ( $Ro \approx 0.1$ ). The color of the profiles denotes the value of  $Ra/Ra_{crit}$ , where  $Ra_{crit}$  is given in Table 1. (e) The ratio of the thicknesses of the dynamical boundary layers ( $\delta_{Ro}$ ) and thermal boundary layers ( $\delta_s$ ) is shown vs.  $Ra/Ra_{crit}$  for fixed  $Ro_p$ . (f)  $\delta_s$  is plotted vs.  $Ra/Ra_{crit}$  in units of the density scale height at the top of the atmosphere ( $H_p$ ). Vertical lines denote when  $\delta_s/H_p = 1$  for each value of  $Ro_p$ .

the  $Ro$  boundary layer ( $\delta_{Ro}$ ) in the same manner. In figure 4e, we plot  $\delta_{Ro}/\delta_s$ , the ratio of the sizes of these two boundary layers. As anticipated, the dynamical boundary layer ( $\delta_{Ro}$ ) becomes relatively thinner with respect to the thermal boundary layer ( $\delta_s$ ) as  $Ro$  and  $Ro_p$  decrease. However, the precise scaling of this boundary layer ratio with  $Ro_p$  and  $Ra$  is unclear, and we cannot immediately compare these ratios to similar measures from the Rayleigh-Bénard convection literature, such as Fig. 5 of King et al. (2013). They measure the dynamical boundary layer thickness as the peak location of the horizontal velocities, but our horizontal velocities are subject to stress-free boundary conditions, and we find that the maxima of horizontal velocities occur precisely at the boundaries. In figure 4f, we plot  $\delta_s$  in units of the density scale height at the top of the atmosphere, and we plot vertical lines when this crosses 1. We find no systematic change in behavior when  $\delta_s$  is smaller than the local density scale height.

#### 4. DISCUSSION

In this letter, we studied low-Mach-number, stratified, compressible convection under the influence of rotation. We examined three paths through  $Ra$ - $Ta$  space, and showed that the newly-defined Predictive Rossby number,  $Ro_p = Ra/(\text{Pr}^{1/2}Ta^{3/4})$ , determines the value of the evolved Rossby number.

Shockingly, along these constant  $Ro_p$  pathways, particularly when  $Ro \lesssim 0.1$ , we find  $Nu \propto Ra^{2/7}$  and  $Re_{||} \propto Ra^{0.45}$ . These scalings are indistinguishable from the scalings of  $Re$  and  $Nu$  with  $Ra$  in non-rotating

Boussinesq convection (Ahlers et al. 2009). The  $Nu$  scaling here is particularly surprising, as Julien et al. (2012) theorized that in the rapidly rotating asymptotic limit,  $(Nu - 1) \propto Ra^{3/2}/Ta = Ro_p^{8/3}Ra^{1/6} \propto (Ra/Ra_{crit})^{1/6}$ , which is much weaker than the  $Ra^{2/7}$  law we find here. Here we have used that  $Ra_{crit} \propto Ro_p^{-16}$ , which can be derived from Eqn. 5 in the large  $Ta$  limit.

At a fixed  $Ta = 10^{14}$ , Stellmach et al. (2014) found that the  $Ra^{3/2}$  scaling described the results of stress-free DNS in Boussinesq cylinders very well. Gastine et al. (2016) studied Boussinesq convection in spherical shells with no-slip boundaries, and also found good agreement with the theory of Julien et al. (2012) for various  $Ra$  at  $Ta \geq 10^{10}$ . We leave it to future work to explain this discrepancy between Boussinesq theory and our observed  $Nu$  vs.  $Ra$  scaling.

In this work, we experimentally arrived at the  $Ra/Ta^{3/4} = RaEk^{3/2}$  scaling in  $Ro_p$ , but this relationship was independently discovered by King et al. (2012). Arguing that the thermal boundary layers should scale as  $\delta_s \propto Ra^{-1/3}$  and rotational Ekman boundary layers should scale as  $\delta_{Ro} \propto Ta^{-1/4} = Ek^{1/2}$ , they expect these boundary layers to be equal in size when  $Ra/Ta^{3/4} \sim 1$ . They demonstrate that when  $2 \lesssim Ra/Ta^{3/4} \lesssim 20$  flows are in the transitional regime, and for  $Ra/Ta^{3/4} \lesssim 2$ , flows are rotationally constrained. We remind the reader that Boussinesq values of  $Ra$  and  $Ta$  are not the same as their values in our stratified domains here, as diffusivities change with depth (see section 2). Taking into account this change with depth, our simulations

fall in King et al. (2012)’s rotationally constrained ( $Ro_p = 0.6$ ) and near-constrained transitional regime ( $Ro_p = \{0.957, 1.58\}$ ). The measured values of  $Ro$  in Fig. 1b and the observed dynamics in Fig. 2 agree with this interpretation.

We note briefly that the scaling  $Ra \propto Ta^{3/4}$  is very similar to another theorized boundary between fully rotationally constrained convection and partially constrained convection predicted in Boussinesq theory, of  $Ra \propto Ta^{4/5}$  (Julien et al. 2012; Gastine et al. 2016). This  $Ta^{4/5}$  scaling also arises through arguments of geostrophic balance in the boundary layers, and is a steeper scaling than the  $Ta^{3/4}$  scaling present in  $Ro_p$ . This suggests that at sufficiently low  $Ro_p$ , a suite of simulations across many orders of magnitude of  $Ra$  will not only have the same volume-averaged value of  $Ro$  (as in Fig. 1b), but will also maintain proper force balances within the boundary layers.

Our results suggest that by choosing the desired value of  $Ro_p$ , experimenters can select the degree of rotational constraint present in their simulations. We find that  $Ro \propto Ro_p^{3.34 \pm 0.07}$ , which is within  $2\sigma$  of the estimate in King et al. (2013), who although defining  $Ro$  very differently from our vorticity-based definition here, find  $Ro \propto Ro_p^{3.84 \pm 0.28}$ . We note briefly that they claim that the value of  $Ro$  is strongly dependent upon the Prandtl number studied, and that low  $Ro$  can be achieved at high  $Pr$  without achieving a rotationally constrained flow. We studied only  $Pr = 1$  here, and leave it to future work to determine if the scaling of  $Ro_p \propto Pr^{-1/4}$  is the correct scaling to predict the evolved Rossby number.

Despite the added complexity of stratification and despite our using stress-free rather than no-slip boundaries, the boundary layer scaling arguments put forth in

King et al. (2012) seem to hold up in our systems. This is reminiscent of what we found in AB17, in which convection in stratified domains, regardless of Mach number, produced boundary-layer dominated scaling laws of  $Nu$  that were nearly identical to the scaling laws found in Boussinesq Rayleigh-Bénard convection.

We close by noting that once  $Ro_p$  is chosen such that a convective system has the same Rossby number as an astrophysical object of choice, it is straightforward to increase the turbulent nature of simulations by increasing  $Ra$ , just as in the non-rotating case. Although all the results reported here are for a Cartesian geometry with antiparallel gravity and rotation, preliminary 3D spherical simulations suggest that  $Ro_p$  also specifies  $Ro$  in more complex geometries (Brown et al. 2019 in prep).

We thank Jon Aurnou and the anonymous referee who independently directed us to the work of King et al. (2012) during the review process, which greatly helped us understand the results of the experiments here. We further thank the anonymous referee for other helpful and clarifying suggestions. This work was supported by NASA Headquarters under the NASA Earth and Space Science Fellowship Program – Grant 80NSSC18K1199. EHA further acknowledges the University of Colorado’s George Ellery Hale Graduate Student Fellowship. This work was additionally supported by NASA LWS grant number NNX16AC92G. Computations were conducted with support by the NASA High End Computing (HEC) Program through the NASA Advanced Supercomputing (NAS) Division at Ames Research Center on Pleiades with allocation GID s1647.

## APPENDIX

### A. TABLE OF SIMULATIONS

Information for select simulations in this work are shown in Table 2. The simulation at minimum ( $Ra$ ,  $Ta$ ) and maximum ( $Ra$ ,  $Ta$ ) for each of the  $Ro_p$ ,  $Ro_c$ , and  $\mathcal{S}$  paths in Fig. 1b are shown. This information for the displayed simulations and all other simulations in this work is included as a .csv file in the supplemental materials.

## REFERENCES

- Ahlers, G., Grossmann, S., & Lohse, D. 2009, *Rev. Mod. Phys.*, 81, 503
- Anders, E. H., & Brown, B. P. 2017, *Physical Review Fluids*, 2, 083501
- Augustson, K. C., Brown, B. P., Brun, A. S., Miesch, M. S., & Toomre, J. 2012, *ApJ*, 756, 169
- Aurnou, J. M., & King, E. M. 2017, *Proceedings of the Royal Society of London Series A*, 473, 20160731
- Brown, B. P., Browning, M. K., Brun, A. S., Miesch, M. S., & Toomre, J. 2008, *ApJ*, 689, 1354
- . 2010, *ApJ*, 711, 424
- Brown, B. P., Miesch, M. S., Browning, M. K., Brun, A. S., & Toomre, J. 2011, *ApJ*, 731, 69
- Brummell, N. H., Hurlburt, N. E., & Toomre, J. 1996, *ApJ*, 473, 494
- . 1998, *ApJ*, 493, 955

**Table 2.** Table of simulation information

Ra <sub>top</sub>	Ta <sub>top</sub>	Ro <sub>p, top</sub>	Ra <sub>mid</sub>	Ta <sub>mid</sub>	Ro <sub>p, mid</sub>	Ro <sub>c</sub>	$\mathcal{S}$	$L_x/L_z$	(nz, nx, ny)	Ro	Re <sub>  </sub>	Re <sub>⊥</sub>	Nu
<b>Constant Ro<sub>p</sub>, path III</b>													
$1.8 \times 10^5$	$4.1 \times 10^7$	0.60	$1.4 \times 10^7$	$3.0 \times 10^9$	1.03	0.067	1.1	0.51	(256, 32, 32)	0.015	19.4	2.5	1.2
$1.2 \times 10^9$	$5.2 \times 10^{12}$	0.60	$9.2 \times 10^{10}$	$3.8 \times 10^{14}$	1.03	0.015	3.0	0.07	(2048, 64, 64)	0.026	1771	32.0	15.4
$5.2 \times 10^2$	$4.6 \times 10^3$	0.96	$3.8 \times 10^4$	$3.4 \times 10^5$	1.64	0.333	1.13	2.28	(64, 64, 64)	0.074	4.2	2.5	1.2
$3.8 \times 10^8$	$3.1 \times 10^{11}$	0.96	$2.8 \times 10^{10}$	$2.3 \times 10^{13}$	1.64	0.035	6.0	0.12	(2048, 64, 64)	0.129	3906	113	66.9
$7.9 \times 10^1$	$1.0 \times 10^2$	1.58	$5.8 \times 10^3$	$7.4 \times 10^3$	2.70	0.888	1.56	4.44	(64, 64, 64)	0.303	4.4	4.9	1.7
$1.4 \times 10^7$	$9.7 \times 10^8$	1.58	$1.0 \times 10^9$	$7.2 \times 10^{10}$	2.70	0.119	10.0	0.30	(512, 128, 128)	0.376	1257	94.9	40.1
<b>Constant Ro<sub>c</sub>, path II</b>													
$8.6 \times 10^4$	$8.6 \times 10^6$	0.74	$6.3 \times 10^6$	$6.3 \times 10^8$	1.26	0.1	1.47	0.68	(128, 128, 128)	0.051	40.2	6.7	2.2
$2.6 \times 10^6$	$2.6 \times 10^8$	1.13	$1.9 \times 10^8$	$1.9 \times 10^{10}$	1.93	0.1	4.64	0.39	(256, 512, 512)	0.27	565	53.2	33.3
$1.4 \times 10^3$	$1.6 \times 10^4$	1.01	$1.1 \times 10^5$	$1.2 \times 10^6$	1.72	0.3	1.47	1.90	(64, 128, 128)	0.124	11.3	5.4	1.8
$1.1 \times 10^6$	$1.2 \times 10^7$	2.29	$7.8 \times 10^7$	$8.6 \times 10^8$	3.93	0.3	14.7	0.65	(192, 384, 384)	0.808	529	83.5	27.3
$5.5 \times 10^1$	$5.5 \times 10^1$	1.65	$4.0 \times 10^3$	$4.0 \times 10^3$	2.82	1.0	1.47	4.84	(64, 128, 128)	0.303	3.6	4.4	1.5
$2.8 \times 10^6$	$2.8 \times 10^6$	6.39	$2.0 \times 10^8$	$2.0 \times 10^8$	10.93	1.0	100	0.82	(256, 512, 512)	3.357	1099	220	46.6
<b>Constant <math>\mathcal{S}</math>, path I</b>													
$1.9 \times 10^1$	$1.1 \times 10^{-1}$	10.00	$1.4 \times 10^3$	$7.9 \times 10$	17.12	13.2	2.0	9.91	(64, 64, 64)	3.668	3.0	10.2	1.7
$3.0 \times 10^6$	$1.1 \times 10^9$	0.70	$2.2 \times 10^8$	$8.1 \times 10^{10}$	1.20	0.052	2.0	0.30	(512, 128, 128)	0.053	242	17.9	6.0
$3.0 \times 10^1$	$2.0 \times 10^{-1}$	10.00	$2.2 \times 10^3$	$1.5 \times 10^1$	17.12	12.2	3.0	9.48	(64, 64, 64)	4.418	5.0	15.5	2.1
$1.3 \times 10^7$	$5.6 \times 10^9$	0.80	$9.7 \times 10^8$	$4.2 \times 10^{11}$	1.37	0.048	3.0	0.23	(512, 128, 128)	0.08	592	33.4	13.6

NOTE—Input parameters and output parameters for select simulations are shown. For each of the eight paths in Fig. 1b, we show information for the lowest and highest (Ra, Ta) point on that path. The first six rows show information for constant Ro<sub>p</sub> paths, the next six for constant Ro<sub>c</sub> paths, and the last four for constant  $\mathcal{S}$  paths. We show the input Ra, Ta, and Ro<sub>p</sub> at the top of the atmosphere, as well as their stratification-weighted values at the midplane of the atmosphere, which provide a more direct comparison to Boussinesq values (Unno et al. 1960). We also provide the input Ro<sub>c</sub> at the top of the atmosphere,  $\mathcal{S}$ , aspect ratio ( $L_x/L_z$ ), and coefficient resolution (nz, nx, ny). Each dimension of the physical grid is 3/2 the size of the coefficient grid for adequate dealiasing of quadratic nonlinear terms. Output values of Ro, Re<sub>||</sub>, Re<sub>⊥</sub>, and Nu are also provided. This table is published in its entirety in a .csv file included in the supplemental materials.

Brun, A. S., Strugarek, A., Varela, J., et al. 2017, *ApJ*, 836, 192

Busse, F. H. 2002, *Physics of Fluids*, 14, 1301

Calkins, M. A., Julien, K., & Marti, P. 2015, *Geophysical and Astrophysical Fluid Dynamics*, 109, 422

Chandrasekhar, S. 1961, *Hydrodynamic and hydromagnetic stability*

Cheng, J. S., Stellmach, S., Ribeiro, A., et al. 2015, *Geophysical Journal International*, 201, 1

Ecke, R. E., & Niemela, J. J. 2014, *PhRvL*, 113, 114301

Featherstone, N. A., & Hindman, B. W. 2016, *ApJ*, 830, L15

Gastine, T., Wicht, J., & Aubert, J. 2016, *Journal of Fluid Mechanics*, 808, 690

Gastine, T., Yadav, R. K., Morin, J., Reiners, A., & Wicht, J. 2014, *MNRAS*, 438, L76

Glatzmaier, G. A., & Gilman, P. A. 1982, *ApJ*, 256, 316

Greer, B. J., Hindman, B. W., & Toomre, J. 2016, *ApJ*, 824, 4

Guerrero, G., Smolarkiewicz, P. K., Kosovichev, A. G., & Mansour, N. N. 2013, *ApJ*, 779, 176

Julien, K., Knobloch, E., Rubio, A. M., & Vasil, G. M. 2012, *Physical Review Letters*, 109, 254503

Julien, K., Legg, S., McWilliams, J., & Werne, J. 1996, *Journal of Fluid Mechanics*, 322, 243

Käpylä, P. J., Käpylä, M. J., & Brandenburg, A. 2014, *A&A*, 570, A43

King, E. M., Stellmach, S., & Aurnou, J. M. 2012, *Journal of Fluid Mechanics*, 691, 568

King, E. M., Stellmach, S., & Buffett, B. 2013, *Journal of Fluid Mechanics*, 717, 449

King, E. M., Stellmach, S., Noir, J., Hansen, U., & Aurnou, J. M. 2009, *Nature*, 457, 301

Schmitz, S., & Tilgner, A. 2009, *PhRvE*, 80, 015305

Soderlund, K. M., Sheyko, A., King, E. M., & Aurnou, J. M. 2015, *Progress in Earth and Planetary Science*, 2, 24

Stellmach, S., Lischper, M., Julien, K., et al. 2014, *PhRvL*, 113, 254501

Unno, W., Kato, S., & Makita, M. 1960, *Publications of the Astronomical Society of Japan*, 12, 192

Zhong, J.-Q., Stevens, R. J. A. M., Clercx, H. J. H., et al. 2009, *Physical Review Letters*, 102, 044502